Atmospheric Environment 180 (2018) 216–225

Contents lists available at ScienceDirect

Atmospheric Environment

journal homepage: www.elsevier.com/locate/atmosenv

# Comparison of atmospheric $CO_2$ mole fractions and source–sink characteristics at four WMO/GAW stations in China

Siyang Cheng[a,b,*], Lingxi Zhou[a,b,**], Pieter P. Tans[c], Xingqin An[a,b], Yunsong Liu[a,b]

[a] State Key Laboratory of Severe Weather, Chinese Academy of Meteorological Sciences (CAMS), Beijing, 100081, China
[b] Key Laboratory of Atmospheric Chemistry, China Meteorological Administration (CMA), Beijing, 100081, China
[c] Earth Systems Research Laboratory, National Oceanic and Atmospheric Administration, Boulder, CO, USA

ARTICLE INFO

*Keywords:*
Atmospheric $CO_2$
Flask sampling observation
GOSAT
Source–sink characteristic
Atmospheric background station

ABSTRACT

As $CO_2$ is a primary driving factor of climate change, the mole fraction and source–sink characteristics of atmospheric $CO_2$ over China are constantly inferred from multi-source and multi-site data. In this paper, we compared ground-based $CO_2$ measurements with satellite retrievals and investigated the source–sink regional representativeness at China's four WMO/GAW stations. The results indicate that, firstly, atmospheric $CO_2$ mole fractions from ground-based sampling measurement and Greenhouse Gases Observing Satellite (GOSAT) products reveal similar seasonal variation. The seasonal amplitude of the column-averaged $CO_2$ mole fractions is smaller than that of the ground-based $CO_2$ at all stations. The extrema of the seasonal cycle of ground-based and column $CO_2$ mole fractions are basically synchronous except a slight phase delay at Lin'an (LAN) station. For the two-year average, the column $CO_2$ is lower than ground-based $CO_2$, and both of them reveal the lowest $CO_2$ mole fraction at Waliguan (WLG) station. The lowest (~4 ppm) and largest (~8 ppm) differences between the column and ground-based $CO_2$ appear at WLG and Longfengshan (LFS) stations, respectively. The $CO_2$ mole fraction and its difference between GOSAT and ground-based measurement are smaller in summer than in winter. The differences of summer column $CO_2$ among these stations are also much smaller than their ground-based counterparts. In winter, the maximum of ground-based $CO_2$ mole fractions and the greatest difference between the two (ground-based and column) datasets appear at the LFS station. Secondly, the representative areas of the monthly $CO_2$ background mole fractions at each station were found by employing footprints and emissions. Smaller representative areas appeared at Shangdianzi (SDZ) and LFS, whereas larger ones were seen at WLG and LAN. The representative areas in summer are larger than those in winter at WLG and SDZ, but the situation is opposite at LAN and LFS. The representative areas for the stations are different in summer and winter, distributed in four typical regions. The $CO_2$ net fluxes in these representative areas show obvious seasonal cycles with similar trends but different varying ranges and different time of the strongest sink. The intensities and uncertainties of the $CO_2$ fluxes are different at different stations in different months and source-sink sectors. Overall, the WLG station is almost a carbon sink, but the other three stations present stronger carbon sources for most of the year. These findings could be conducive to the application of multi-source $CO_2$ data and the understanding of regional $CO_2$ source–sink characteristics and patterns over China.

## 1. Introduction

$CO_2$ contributes more than 50% of the total climate forcing caused by long-lived greenhouse gases, which is the primary driving factor of climatic changes involving surface temperature, hydrological cycle, sea level rise, and extreme weather events (IPCC-AR5, 2013). The global average tropospheric mole fraction of monthly $CO_2$ was approximately 404 parts per million (ppm) in April 2016, and the rate of increase was at a record high during 2015 and 2016 (www.esrl.noaa.gov/gmd/ccgg/trends/). The anthropogenic $CO_2$ emissions from fossil-fuel combustion and cement production amounted to approximately 9.1 PgC in 2010, and about 55% of these emissions were absorbed by the terrestrial ecosystem and ocean (Ballantyne et al., 2012; Peters et al., 2011). As unprecedented population growth and resource consumption have led to highly increased $CO_2$ emissions since the early 1980s, it is significant to understand further the patterns of atmospheric $CO_2$ mole fraction and source–sink characteristics over China through multi-source and multi-site data (Piao et al., 2009; Zhang et al., 2014c).

* Corresponding author. Chinese Academy of Meteorological Sciences (CAMS), Beijing, 100081, China.
** Corresponding author. Chinese Academy of Meteorological Sciences (CAMS), Beijing, 100081, China.
*E-mail addresses:* sycheng@cma.gov.cn (S. Cheng), zhoulx@cma.gov.cn (L. Zhou).

https://doi.org/10.1016/j.atmosenv.2018.03.010
Received 30 August 2017; Received in revised form 2 March 2018; Accepted 5 March 2018
Available online 05 March 2018
1352-2310/ 

The mole fraction of $CO_2$ is almost the same everywhere, but relatively small differences, especially near the surface, are caused by recent emissions and removals (Zhang et al., 2013b). The variation and source–sink characteristics of $CO_2$ over China have been investigated by using observation data from different platforms and statistical data (Xu et al., 2017). In the framework of the World Meteorological Organization's Global Atmosphere Watch (WMO/GAW), atmospheric greenhouse gases have been observed continuously at four background stations in China (WLG: Waliguan, SDZ: Shangdianzi, LAN: Lin'an, LFS: Longfengshan) (Fang et al., 2014; Liu et al., 2009; Zhou et al., 2006). The traceable, comparable, and high-precision $CO_2$ data obtained at these stations have been used widely in many studies, such as source–sink inversion studies (Jiang et al., 2013; Zhang et al., 2014a). Although the variation of $CO_2$ mole fraction can be obtained accurately by the WMO/GAW network of ground stations, this measurement with sparse spatial coverage is time consuming and easily affected by surrounding environment (Liu et al., 2014). Satellite remote sensing has been used to monitor $CO_2$ column mole fraction since 2002 because it has the advantages of spatial coverage, speed, and continuity (Boesch et al., 2011; Buchwitz et al., 2004; Clerbaux et al., 2009; Jiang et al., 2010; Kulawik et al., 2010; Tangborn et al., 2013; Xu et al., 2017; Yokota et al., 2009; Zhang et al., 2015). However, satellite retrievals of $CO_2$ (and other greenhouse gases) cannot be calibrated. They are only useable if systematic biases, many of which remain unknown, can be reduced to extremely low levels, to less than 0.1 ppm in the case of $CO_2$ (Fang et al., 2016; Masarie et al., 2001). Several detectors have been launched into space, including the Atmospheric Infrared Sounder (AIRS), the Scanning Imaging Absorption Spectrometer for Atmospheric Cartography (SCIAMACHY), the Greenhouse Gases Observing Satellite (GOSAT), the second Orbiting Carbon Observatory (OCO-2), and the Chinese Carbon Dioxide Observation Satellite (TanSat) (Aumann et al., 2003; Bovensmann et al., 1999; Chen et al., 2017; Frankenberg et al., 2015; Kuze et al., 2009). The retrievals from these satellites need to be compared to calibrated in-situ (at the surface and in the vertical column) measurements to discover, and then eliminate, retrieval biases. Currently, atmospheric transport models are used to combine the two types of data and study their level of compatibility, but this method has its own limitations because transport model biases cause discrepancies in addition to those between the two types of data (Baker et al., 2010; Chevallier et al., 2009, 2011; Cogan et al., 2012; Houweling et al., 2004; Jiang et al., 2013; Lauvaux et al., 2009; Miller et al., 2007; Nassar et al., 2011; Peters et al., 2007; Pillai et al., 2010; Reuter et al., 2011; Streets et al., 2013; Zhang et al., 2014a). Here, we use satellite retrievals of atmospheric $CO_2$ over four WMO/GAW stations in China to reveal the $CO_2$ pattern and assess the coherence of different datasets (Zhou et al., 2013).

The pattern of $CO_2$ mole fraction at each station is highly correlated to the source and sink characteristics of $CO_2$ in a specific area, which is called “source–sink regional representativeness.” The key for this representativeness is to find the representative area, which has been explored at the WLG station through simulation results (Cheng et al., 2017a). The representative area and source–sink characteristics of this area are important for understanding the regional differences of $CO_2$ mole fraction, evaluating the site layout, and developing emission reduction strategies because of the differences in the stage of economic development and the diverse climates in China (Xu et al., 2017). Some studies have focused on the representativeness of fluxes, radiation, temperature, and air pollutants (e.g., Xu et al., 2015). Researches on the patterns and sources of $CO_2$ mole fraction at the WMO/GAW stations in China have also been conducted by using the method of isotope tracing and individual trajectories (Xia et al., 2015; Zhang and Zhou, 2013). However, to the best of our knowledge, there are no comparison studies on the representative areas of $CO_2$ background mole fractions at the four WMO/GAW stations in China, as well as the source–sink characteristics in the representative areas.

This study aims to examine the variation of $CO_2$ mole fractions using calibrated in-situ sampling observations and the GOSAT retrieval products and compare the source–sink regional representativeness of the $CO_2$ background mole fractions at China's four WMO/GAW stations. Section 2 introduces the sites, $CO_2$ sampling, GOSAT products, and the statistical analysis methods for source–sink regional representativeness. Section 3 presents the results with discussion and consists of two parts: (1) a comparison of $CO_2$ mole fraction between the surface observations at the four WMO/GAW stations and the GOSAT products and (2) an evaluation of the representative areas of $CO_2$ background mole fractions and a comparison of the source–sink characteristics corresponding to the $CO_2$ background mole fractions at the four WMO/GAW stations. Finally, the summary and conclusions are presented in Section 4.

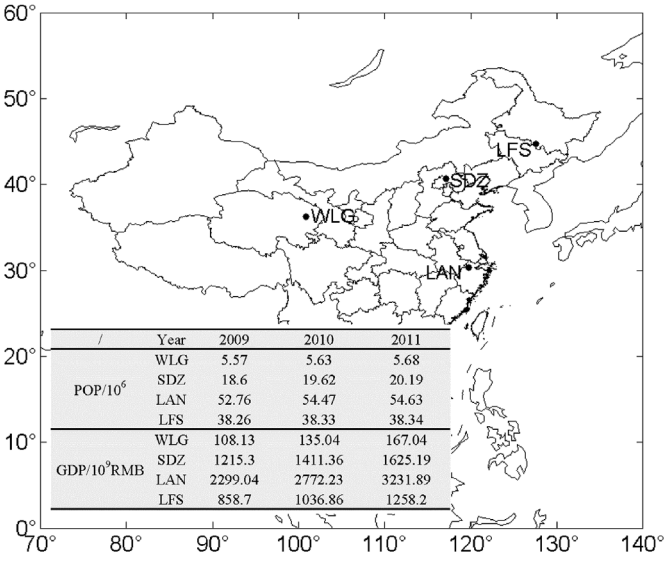


| / | Year | 2009 | 2010 | 2011 |
|---|---|---|---|---|
| POP/$10^6$ | WLG | 5.57 | 5.63 | 5.68 |
| | SDZ | 18.6 | 19.62 | 20.19 |
| | LAN | 52.76 | 54.47 | 54.63 |
| | LFS | 38.26 | 38.33 | 38.34 |
| GDP/$10^9$RMB | WLG | 108.13 | 135.04 | 167.04 |
| | SDZ | 1215.3 | 1411.36 | 1625.19 |
| | LAN | 2299.04 | 2772.23 | 3231.89 |
| | LFS | 858.7 | 1036.86 | 1258.2 |

**Fig. 1.** Geographical locations of the four WMO/GAW stations in China (black dots). The population (POP) and gross domestic product (GDP) in the affiliated provinces are shown in the inserted table.

## 2. Data and methods

### 2.1. Sites and $CO_2$ sampling observations

Atmospheric $CO_2$ samples were collected by flasks during 2009–2011 at the four stations of the WMO/GAW network in China (Fig. 1). The population and gross domestic product (http://data.stats.gov.cn/) of the provinces affiliated with these sites are also shown by the table inserted into Fig. 1. These stations are global or regional background stations, representing atmospheric conditions in different climate features, vegetation types, and economic zones in China (Fang et al., 2014; Liu et al., 2009).

The WLG station (36°17′ N, 100°54′ E; 3810 m asl) is located on the northeastern edge of the Tibetan Plateau (Liu et al., 2014). This station is isolated from industrial and population centers. Yak and sheep grazing is the main economic activity in summer. The area surrounding the WLG station has maintained its natural environment of arid/semi-arid grassland and desert steppe and has a typical plateau continental climate with predominant wind directions of southwest in winter and northeast/southeast in summer (Zhang et al., 2013a; Zhou et al., 2005).

The SDZ station (40°39′ N, 117°07′ E; 293 m asl) is about 120 km northeast of Beijing. The area surrounding the SDZ station consists primarily of shrubs, orchards, and farmland. No large industrial zone exists within 30 km of the station. The dominant wind directions are ENE in autumn and winter and WSW in spring and summer (An et al., 2012).

The LAN station (30°18′ N, 119°44′ E; 138.6 m asl) lies on the top of a hill in Zhejiang Province and is surrounded by forest, farming areas,

and hilly land with a humid subtropical monsoon climate. There are no large villages within 3 km of the station. The prevailing winds there are northeasterly and southwesterly winds (Pu et al., 2014).

The LFS station (44°44′ N, 127°36′ E; 330.5 m asl) is located on the top of Mt. Longfengshan in Heilongjiang Province. Agricultural areas lie to the north and west of LFS, and extensive forested land exists to its east and south. No large cities or industrial zones exist within 40 km of the station. LFS is dominated by a temperate continental monsoon climate (Liu et al., 2009).

At the four stations mentioned above, discrete surface $CO_2$ data from flask sampling and analysis have been obtained through the method recommended by WMO/GAW (Liu et al., 2014). To ensure the quality of the samplings, the flask is subjected to a 24 h vacuum test, filled with dry balance gas, flushed with local air, and then pressurized to ~6.5 psi above ambient pressure. Sampling begins in the morning (~8:00) local time at the WLG station and in the afternoon (~14:00) at the other three regional stations when atmospheric conditions are suitable for capturing "background" characteristics (Liu et al., 2009). Air samples, collected approximately weekly, are transported to the Greenhouse Gases Research Laboratory of the China Meteorological Administration (CMA) for analysis. Generally, the $CO_2$ mole fractions are determined by a cavity ring down spectroscopy system (a non-dispersive infrared spectroscopy observation system before October 2009). The $CO_2$ values are calibrated by the reference gas and working high and low standard gases, which are traceable to the WMO X2007 standard scale. Due to sampling, storage, or measurement problems, $CO_2$ selection is an important part of the data post-processing, such as for quality control, screening, and curve-fitting. Partially because of its simplicity, the $CO_2$ dataset from flask sampling is reliable and internationally comparable with high precision (Fang et al., 2015a; Li et al., 2014; Masarie et al., 2001; Tans et al., 1989; Xia et al., 2015; Zhou et al., 2003).

### 2.2. GOSAT products

Designed specifically to retrieve the mole fractions of greenhouse gases (e.g., $CO_2$), the Greenhouse Gases Observing Satellite (GOSAT) was launched to sun-synchronous orbit in 2009. It observes a same place every three recurrent days. Column-averaged $CO_2$ dry air mole fraction can be retrieved from the shortwave infrared bands recorded by the sensor of the Fourier transform spectrometer (FTS) onboard GOSAT (Miao et al., 2013). The optimal estimation retrieval algorithm is used to obtain GOSAT Level 2 (L2) products (O'Dell et al., 2012; Yoshida et al., 2011), estimating column-averaged $CO_2$ over a specific observation point and at a specific time. The GOSAT Level 3 (L3) products, providing a monthly global distribution of column $CO_2$ (2.5 × 2.5 degrees of grid as a unit), are generated by applying statistical processing to the FTS L2 products. The data products (V02.xx) derived from GOSAT observations have approximately a 2 ppm standard deviation when compared with ground-based observations and in situ airborne measurement data (Lei et al., 2014). The GOSAT L2/L3 data products (V02.21), available at http://data2.gosat.nies.go.jp/index_en.html, were used in this study.

### 2.3. Source–sink regional representativeness analysis

For the $CO_2$ background mole fractions at monthly scale at the four WMO/GAW stations in China, a statistical method was used to explore their source–sink regional representativeness. The key to the method is to determine the area where maximum correlation exists between time series of atmospheric $CO_2$ mole fractions and regional emissions. The representative source–sink regions can be found through simulations of the FLEXible PARTicle dispersion model (FLEXPART) and the Carbon Tracker 2015 model (CT2015). The method is carried out in following steps.

Firstly, an emission sensitivity function or transport climatology is calculated by 3-hourly backward simulation of FLEXPART (Stohl et al., 2005). As most emissions appear in the layer adjacent to the surface, the emission sensitivity function in this layer is of particular interest and is here abbreviated as "Footprint," which is determined by the particle residence time in grid cell and denotes the influence of the potential source on the observation site. Footprint $s(m)$ with $1^\circ \times 1^\circ$ horizontal resolution, corresponding to the $m^{\text{th}}$ $CO_2$ mole fraction, can be calculated by releasing 50,000 particles at the observation site during the 3-hourly interval and following them backward for 7 days. There is a one-to-one correspondence between footprints and $CO_2$ mole fractions. If the number of selected $CO_2$ data in one month is $M$, the monthly footprint $s_{mon}(i, j)$ in a particular surface grid cell $(i, j)$ is calculated as

$$s_{mon}(i,j) = \sum_{m=1}^{M} s(i,j,m) \tag{1}$$

where $s_{mon}(i, j)$ represents the frequency of air masses in grid cell $(i, j)$ arriving at the observation site. Based on the variable $s_{mon}(i, j)$, we assume a threshold value $(T_r)$ of footprint and define a logic matrix $L_{mon}(i, j)$ as the mask grid.

$$L_{mon}(i,j) = \begin{cases} 1 & s_{mon}(i,j) \geq T_r \\ 0 & s_{mon}(i,j) < T_r \end{cases} \tag{2}$$

Secondly, the spatial and temporal distributions of gridded $CO_2$ fluxes and mole fractions can be retrieved by the CT2015 model using the "top-down" method (Peters et al., 2007). The Carbon Tracker (CT) model, updated approximately once a year, is a $CO_2$ measurement and modeling system that tracks $CO_2$ emissions to the atmosphere (sources) and removals from the atmosphere (sinks) around the world (http://www.esrl.noaa.gov/gmd/ccgg/carbontracker/). The sources and sinks of $CO_2$ consist of four sectors in CT2015: land biosphere ("bio"), wildfire ("fires"), fossil fuel emissions ("ff"), and ocean ("ocean"). At a specific time and place, the simulated $CO_2$ mole fraction $(c)$ is contributed by the initial well-mixed $CO_2$ mole fraction and the transport of fluxes from all global regions for a past period of time (Jiang et al., 2013; Zhang et al., 2014a). According to the time of selected $CO_2$ values, the monthly net fluxes $F_{mon}(i, j)$ [mol/(m$^2$·s)] in each grid cell can be extracted from the CT2015 model. Both $L_{mon}$ and $F_{mon}$ are global 180 × 360 grids/matrices (latitude × longitude). Hence, monthly regional emissions can be calculated as

$$E_{area} = \sum_{i=1}^{180} \sum_{j=1}^{360} a(i,j) F_{mon}(i,j) L_{mon}(i,j) \tag{3}$$

where $a(i, j)$ is the area of the $(i, j)^{\text{th}}$ grid.

Finally, the correlation coefficient $(r)$ of the time series of regional emissions $(E_{area})$ and $CO_2$ mole fractions $(c)$ at each station on a monthly scale can be calculated iteratively on the basis of different threshold values of footprint. As a result, the best footprint threshold value $(T_R)$ and the maximum correlation $(R)$ can be found through correlation analysis and numerical iteration. The representative source–sink region is confined by the best footprint threshold value as follows:

$$L_{mon,T_R}(i,j) = L_{mon}(i,j) \quad (T_r = T_R) \tag{4}$$

which shows the area where emissions have the greatest influence on the atmospheric $CO_2$ mole fractions in a particular month for a specific observation station. The area of the representative source–sink region is:

$$A = \sum_{i=1}^{180} \sum_{j=1}^{360} a(i,j) L_{mon,T_R}(i,j) \tag{5}$$

Based on the emission and the area of the representative source–sink region, regional fluxes $F_{area}$ can be estimated:

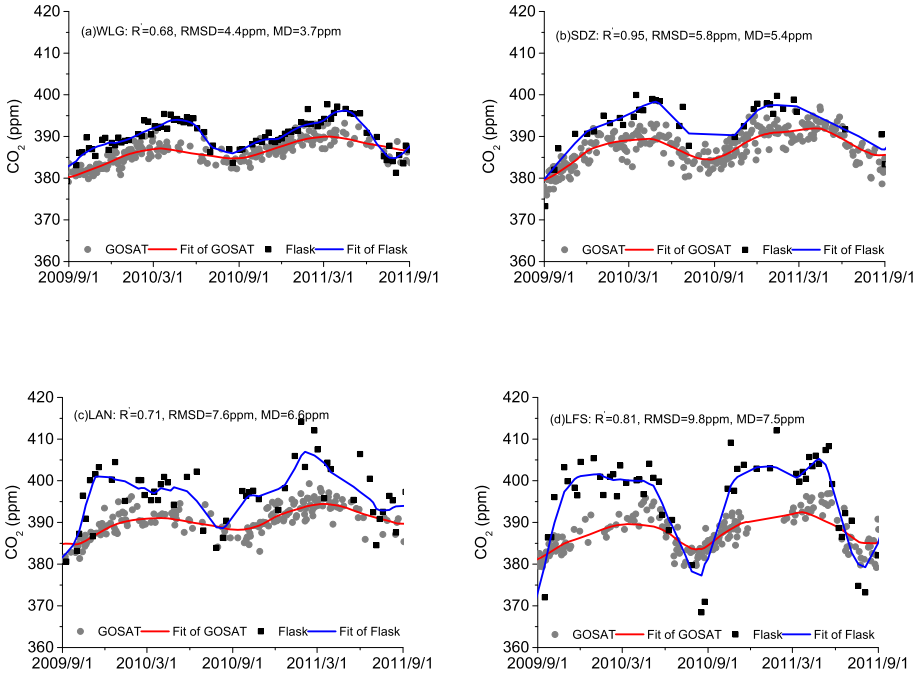


**Fig. 2.** Comparison of $CO_2$ mole fraction between flask sampling observation (black squares) and GOSAT L2 product (gray dots) at China's four WMO/GAW stations. Blue and red lines are fitting curves. R′, RMSD, and MD denote the correlation coefficient, root mean square difference, and mean difference (Flask minus GOSAT), respectively, between the fitting $CO_2$ mole fractions of the two datasets.

$$F_{area} = E_{area}/A \quad (6)$$

The different sectors ($k$) of source and sink in the representative source–sink region [$F_{mon,k,T_R}(i,j)$] can also be obtained by:

$$F_{mon,k,T_R}(i,j) = F_{mon,k}(i,j)L_{mon,T_R}(i,j) \quad (7)$$

## 3. Results and discussion

### 3.1. Contrast analysis of $CO_2$ sampling observation and GOSAT product

#### 3.1.1. Comparison of GOSAT L2 product with $CO_2$ mole fraction derived from the four WMO/GAW stations in China

Fig. 2 shows the qualified $CO_2$ mole fractions from September 2009 to August 2011 at the WLG, SDZ, LAN, and LFS stations in China, separately obtained from flask sampling and GOSAT L2 products. If more than one data point is available at a given station in a day, it is averaged. The GOSAT data were selected when horizontal distance between a given station and the geographic location of a GOSAT measurement was less than 500 km. Relatively, fewer GOSAT $CO_2$ data can be collected at LAN in summer and at LFS in winter, which may be attributed to the influence of the cloud, the locations of the two stations, and data selection procedures of GOSAT. GOSAT does not work for high latitudes in winter, because FTS SWIR (ShortWave InfraRed) requires sunlight with the Sun sufficiently high above the horizon (Bréon and Ciais, 2010). In order to decrease the uncertainty of a single measurement, the $CO_2$ mole fractions were smoothed by the curve-fitting method of Thoning et al. (1989) (Fig. 2).

The two datasets, from flask sampling and GOSAT, presented similar patterns of seasonal variation at all four stations. The correlation coefficient R′ ranges from 0.68 (WLG site) to 0.95 (SDZ site). The minimum $CO_2$ mole fraction appears in late summer and the maximum occurs in spring or winter. Seasonal variations of atmospheric $CO_2$ at the four WMO/GAW stations are dominated mainly by the exchange with the land biosphere. The occurrence time of the seasonal $CO_2$ maximum is related to human activities, different regional terrestrial ecosystems, and local meteorological conditions (Fang et al., 2014).

The mean differences (MD = 3.7–7.5 ppm) are positive at the four stations, probably because the two datasets separately provide $CO_2$ dry air mole fractions at the surface and estimates of the $CO_2$ column-averaged dry air mole fractions. The column-averaged $CO_2$ mole fractions are manifest in the lower amplitude of the seasonal cycle which is produced at the surface and attenuated at higher altitudes (Jiang et al., 2016). A slight phase delay can also be expected, but this is not very clear except at LAN station from Fig. 2. It can be further identified by the fact that the ground-based $CO_2$ is significantly less than the column $CO_2$ in summer because of the strong uptake by rice plants and forests at LFS.

There are some differences in $CO_2$ mole fractions among these stations. For ground-based $CO_2$, the seasonal amplitudes (peak-to-peak value) range in a diminishing sequence from LFS, SDZ, LAN, to WLG. Differing from the regional background stations of LAN and LFS, the maximum of $CO_2$ mole fractions at WLG is low, which may be due to the site's high altitude and its location far from industrial zones and large cities (Liu et al., 2009). The biggest R′ = 0.95 and RMSD = 9.8 ppm appear at SDZ and LFS stations, respectively. WLG station presents the smallest values of R′ = 0.68, RMSD = 4.4 ppm, and MD = 3.7 ppm. So, generally speaking, the characteristics of GOSAT column $CO_2$ are similar to the ground-based $CO_2$, but the differences of the seasonal amplitudes and levels of GOSAT column $CO_2$ among these stations are smaller.

#### 3.1.2. Spatial distribution of atmospheric $CO_2$ mole fractions

There is a higher spatial coverage for the current GOSAT $CO_2$ measurement, although the accuracy and precision of GOSAT $CO_2$ mole fraction are lower than those of the surface flask sampling observation. The spatial distributions of column $CO_2$ over China in summer and winter as well as in the two years (September 2009–August 2011) were extracted from the GOSAT L3 products (Fig. 3). The whitened portions in the figure represent places where data do not exist within the range of 500 km from the processed points. The difference of the GOSAT column $CO_2$ spatial distribution is significant over China, with low mole fractions in summer and high mole fractions in winter. In summer, higher $CO_2$ mole fractions are concentrated mainly in the southern and eastern coastal regions of China, while lower values are distributed in Inner Mongolia and Northeast China. However, column $CO_2$ is higher in most parts of China in winter, except for Qinghai and parts of Tibet, Gansu, and Inner Mongolia. From the two-year average (Fig. 3c), the column $CO_2$ distribution presents a significant spatial gradient from east to west, with $CO_2$ mole fractions distributing from high to low, respectively. This pattern is consistent with the result retrieved from

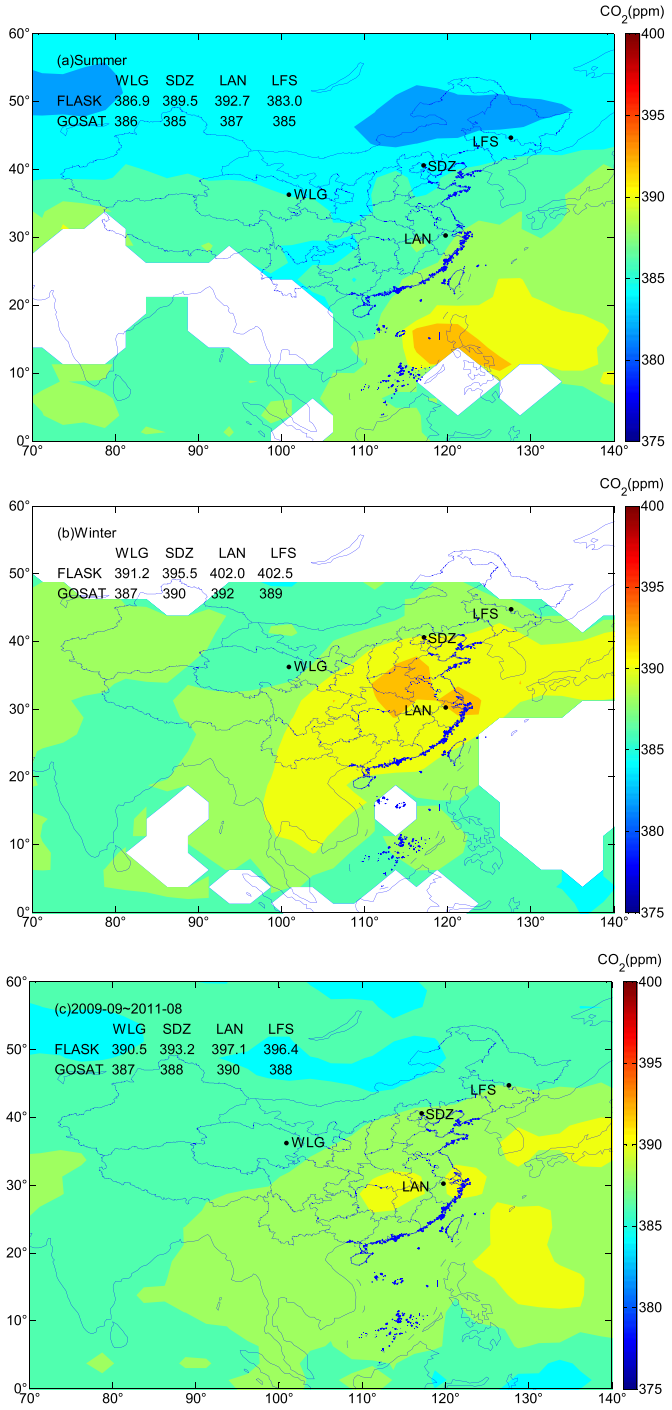


**Fig. 3.** Spatial distribution of $CO_2$ mole fractions from GOSAT L3 products (a) in summer (June, July, August) and (b) in winter (December, January, February) and (c) in September 2009–August 2011. Black dots denote the four WMO/GAW stations. Overlain tables show the mean $CO_2$ mole fractions from flask sampling at these stations and the matching grid cells of GOSAT retrievals.

SCIAMACHY, and the seasonal differences may be connected with regional Normalized Difference Vegetation Index (NDVI) and air temperature (Wang et al., 2015).

The mean $CO_2$ mole fractions from the sampling measurement at the four WMO/GAW stations and the matched grids (2.5° × 2.5°) of GOSAT L3 product are also shown by the overlain tables, respectively (Fig. 3). For the two-year average (Fig. 3c), full column $CO_2$ is lower than $CO_2$ mole fraction adjacent to the surface, but the difference between them remained approximately within the region of 4–8 ppm at these WMO/GAW stations. The $CO_2$ mole fraction at the WLG station is the lowest among the four stations, whether for flask sampling or for GOSAT retrievals. The largest differences (~8 ppm) of $CO_2$ mole fraction between flask data with GOSAT appear at LFS station.

In summer (Fig. 3a), full column $CO_2$ is lower than $CO_2$ mole fraction observed by flask sampling at all stations except LFS. Compared with the values in winter or the two-year average, the $CO_2$ mole fraction and its difference between full column and surface are smaller in summer. The maximum and minimum $CO_2$ mole fraction in the two datasets occur at LAN and LFS, respectively, but the differences of full column $CO_2$ at these stations are much smaller than those of their surface counterpart. In winter (Fig. 3b), full column $CO_2$ is lower than ground-based $CO_2$. The maximum of ground-based $CO_2$ mole fractions and the largest difference between the two datasets appear at the LFS station, perhaps due to heating in Northeast China.

Overall, we estimate that there may be stronger anthropogenic emissions at the SDZ and LAN stations and weaker sinks at the WLG station, i.e., weaker sources at the WLG and LFS stations but stronger sinks at the SDZ, LAN and LFS stations. The estimation of stronger terrestrial $CO_2$ sinks at regional background stations can be confirmed by the distribution of gross primary production (Sun et al., 2018). This is also consistent with previous studies in the southeast and northeast China (Liu et al., 2012; Zhang et al., 2014b).

### 3.2. Source–sink regional representativeness

The spatial and temporal patterns of atmospheric $CO_2$ mole fractions are closely related to $CO_2$ source and sink as well as the transport of the atmosphere. Based on the steps of the statistical method introduced in Section 2.3 and the simulations of FLEXPART and CT2015, the source–sink regional representativeness of the atmospheric $CO_2$ background mole fractions at the four WMO/GAW stations in China were compared.

#### 3.2.1. Footprint

The footprints for summer and winter at the four WMO/GAW stations indicate the sensitivity to surface emissions during the transport of the previous 7 days (Fig. 4). The description “7 days” is a compromise between the enough large spatial coverage and the calculation time of footprint simulation (An et al., 2014). An emission area with a higher footprint value has a larger impact on the observation site. There are pronounced differences between summer and winter footprints for all four sites, which are closely related to the seasonal transition of air mass transport over China. Due to the influence of summer monsoon, the high footprint values (> 4) at WLG in summer are distributed mainly in western China, although air masses from Southeast Asia and the Bay of Bengal play a role in the atmospheric $CO_2$ mole fraction (Xu et al., 2013). The high footprint values (> 4) in winter are concentrated to the west of the WLG station, which is a consequence of the dominant westerlies and consistent with atmospheric transport patterns for a large area of western China (Li et al., 2014). At the SDZ station, the high footprint values (> 4) are distributed mainly in its southeast and northwest in summer and in its northwest in winter, which is probably associated with the Pacific Subtropical High in summer and the Siberian High in winter, respectively. The distribution of high footprint values (> 4) at LAN in summer is related to clean air masses from the sea, but relatively colder air masses containing $CO_2$ emitted in the east of China are prone to reach the LAN station in 7 days in winter (Cheng et al., 2017b). The high footprint values (> 4) at LFS in summer, with a distribution similar to that at the LAN station, are distributed mainly in Northeast China, northeastern Inner Mongolia, and the Sea of Japan, but the high values (> 4) in winter are primarily limited to the northwest of the LFS station. The footprint distributions at three regional stations (SDZ, LAN, and LFS) are similar to some degree in winter because of the effect of northwesterly air flows. Therefore, along with the atmospheric circulation switching between seasons, there are

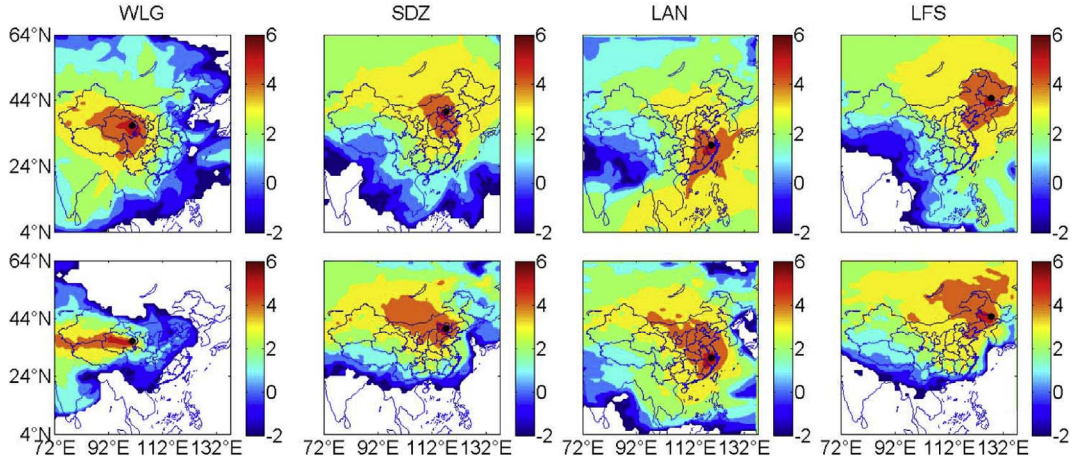


**Fig. 4.** Footprint distributions in logarithmic units ($log_{10}$s) for summer (top row) and winter (bottom row) of 2009 at the WMO/GAW stations. Black dot represents the location of station.

different potential source areas for the four WMO/GAW stations (An et al., 2014; Lu et al., 2012).

### 3.2.2. Data verification and screening

Before the $CO_2$ background extraction from CT2015 simulation results, the results were compared with surface observation values at the four WMO/GAW stations. We used the simulated $CO_2$ mole fractions with a 3° × 2° horizontal grid for a 3-h interval in the vertical layer adjacent to the surface. Outliers in simulation appear because of the "model data mismatch" (MDM), which can be described in different ways and partly defines the rejection criterion (Zhang et al., 2014a, 2014b). In the post-processing of the $CO_2$ simulation data, we eliminated outliers when the simulation results exceeded the range of monthly observed average $CO_2$ mole fraction ± 3 times the standard error of the monthly mean. We selected the qualified $CO_2$ simulation results and matched them with the sampling observations within 1.5 h in the grid cells of each station. Fig. 5a shows the linear regression analysis of atmospheric $CO_2$ mole fractions between observation and simulation at the four WMO/GAW stations from March 2008 to February 2011. The correlation coefficient $R''^2$ at each station ranges from 0.68 (LAN site) to 0.88 (WLG and SDZ sites). The slope of the linear fitting is close to 1 for all stations. Fig. 5b presents the residuals (simulation minus observation) of $CO_2$ mole fractions at each station. The fluctuations of the residual are smaller at WLG and SDZ stations than at the other two stations from the aspect of the 10th (90th) and the 25th (75th) percentiles. The median and mean values of residuals are less than 2 ppm at the four WMO/GAW stations. The bigger deviations mostly appear in the highest and lowest $CO_2$ mole fractions between observations and simulations. In spite of this, previous studies showed that there are no significant differences in capturing the background variation at these stations as a whole through the low-resolution (3° × 2°) and high-resolution (1° × 1°) simulations (Cheng et al., 2013). So it is possible that the patterns of atmospheric $CO_2$ background mole fraction near the surface can be extracted from the CT2015 results.

The atmospheric $CO_2$ background mole fractions at a specific station reflect the regional atmospheric conditions, which can be obtained from the qualified $CO_2$ simulation results above. There are many different approaches for filtering time series of $CO_2$ data (Fang et al., 2015b). With the statistical extraction method of Robust Extraction of Background Signal (REBS), the qualified time series of simulated $CO_2$ mole fractions can be screened into background and non-background (Ruckstuhl et al., 2012). We selected the $CO_2$ background mole fractions from March 2009 to February 2010 (Fig. 6), which were smoothed by the curve-fitting method of Thoning et al. (1989). The bandwidth was set to 60 days in the algorithm of REBS until the differences between $CO_2$ background mole fractions and fitted values were within 2 times the standard deviation of the $CO_2$ simulation background.

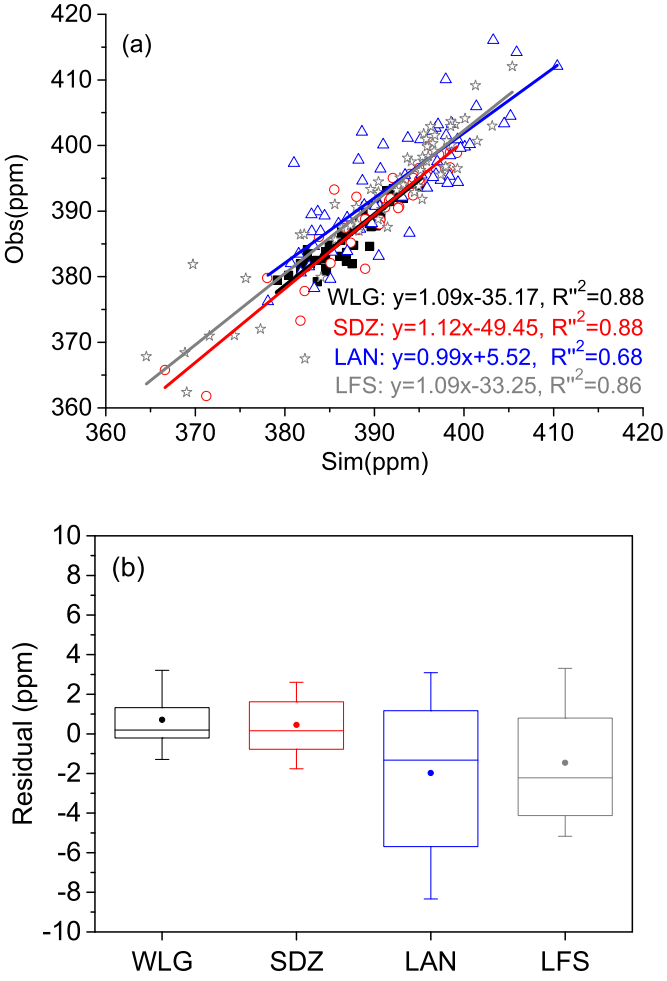


**Fig. 5.** Comparison of $CO_2$ mole fractions between single flask sampling observation and CT2015 simulation from March 2008 to February 2011: (a) linear regression analysis of $CO_2$ mole fractions at WLG (black), SDZ (red), LAN (blue), and LFS (gray); (b) Lower (upper) error bars, boxes, hyphens inside the boxes, and circles are the 10th (90th), 25th (75th) percentiles, the medians, and the mean values of the residuals (simulation minus observation) of $CO_2$ mole fractions at each station, respectively.

However, the seasonal $CO_2$ background trends at the four WMO/GAW stations could be well captured by the "fitting curve". For example, the maximum and minimum seasonal fluctuations appear at the LFS and WLG stations, respectively, matching the observation. The minimum of $CO_2$ mole fractions occurs about in August because of stronger

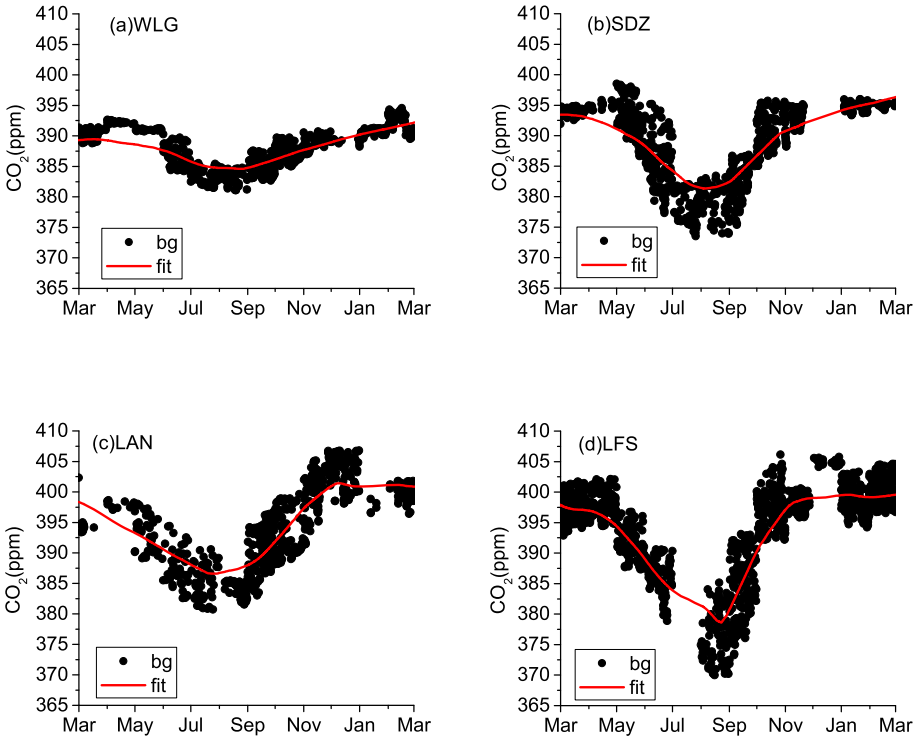


**Fig. 6.** Simulated $CO_2$ background mole fractions ("bg") and fitting curves ("fit") obtained by screening the qualified CT2015 data at the WMO/GAW stations.

photosynthesis of plants in the growing season, and the maximum occurs in spring or winter (Li et al., 2017). The monthly average of the fitted results is used as specific time series to study the source–sink regional representativeness of $CO_2$ background mole fractions at the four WMO/GAW stations in the following.

### 3.2.3. Representative area

According to the method of source–sink regional representativeness, we obtained the areas where the source and sink have the greatest impact on the monthly $CO_2$ fitted background mole fractions at the four WMO/GAW stations. In the process of statistical analysis, we used the monthly average data of $1^\circ \times 1^\circ$ footprints from FLEXPART and $1^\circ \times 1^\circ$ fluxes from CT2015 during the period from March 2009 to February 2010. The representative source–sink area was estimated through the best footprint threshold value. After a series of iterative calculations and correlation analysis, the best footprint threshold values ($T_R$) and the maximum correlation coefficients (R) were separately determined at the four WMO/GAW stations, as shown in Table 1. The area (A) of the best threshold region, where there is maximum correlation between regional $CO_2$ emissions and atmospheric $CO_2$ background mole fractions at each station on a monthly scale, was calculated by Eq. (5). The maximum correlation coefficients ranged from 0.73 (WLG) to 0.94 (LFS). The larger of the best footprint threshold values appeared at the SDZ and LFS stations, corresponding to the smaller areas of the best threshold region. At WLG and LAN, the time series of atmospheric $CO_2$ background mole fractions represented larger space with the smaller of the best footprint threshold values.

**Table 1**
Source–sink regional representativeness for the monthly $CO_2$ fitted background mole fractions from CT2015 at the WMO/GAW stations.

| Representativeness | R | $T_R$ ($\log_{10}$s) | A ($10^6$ km$^2$) | |
|---|---|---|---|---|
| | | | summer | winter |
| WLG | 0.73 | 1.5 | 2.160 | 1.530 |
| SDZ | 0.78 | 2.8 | 0.180 | 0.123 |
| LAN | 0.87 | 1.6 | 2.070 | 2.980 |
| LFS | 0.94 | 2.4 | 0.135 | 0.389 |

The areas of the best threshold region in summer and in winter are also presented in Table 1. The source–sink regional representativeness of atmospheric $CO_2$ background mole fractions, i.e., the best threshold area, changes with the seasons at a specific site, depending on the variation of atmospheric circulations. The representative areas are larger in summer than in winter at the WLG and SDZ stations, but the situations are opposite at the LAN and LFS stations. There are larger differences of best threshold area between summer and winter at the WLG ($6.3 \times 10^5$ km$^2$) and LAN ($-9.1 \times 10^5$ km$^2$) stations. The maximum and minimum source–sink regional representativeness occur at the WLG and LFS stations in summer, respectively, but separately appear at the LAN and SDZ stations in winter. Due to different attributions, the extrema of representativeness and atmospheric $CO_2$ background mole fraction are not always synchronous. According to the differences of the best footprint threshold values, the distributions of best threshold area are significantly different whether in summer or winter or among different stations. To the best of our knowledge, no researches directly compare the representative areas at these stations, but the results above are qualitatively comparable with back-trajectory analyses of the source of $CO_2$ (An et al., 2012; Fang et al., 2015a, 2015b; Zhang and Zhou, 2013). On the whole, the monthly atmospheric $CO_2$ background mole fractions from March 2009 to February 2010 at the four WMO/GAW stations mainly reflect variations of the sources and sinks in the best threshold area. Although the best threshold areas cover many regions in China, additional observation sites are needed to evaluate the $CO_2$ condition.

### 3.2.4. Source and sink in representative region

Fig. 7a shows the monthly averages and standard deviations of $CO_2$ fluxes from March 2009 to February 2010 in the best threshold area, closely associated with the sources and sinks of atmospheric $CO_2$ background mole fractions at the four WMO/GAW stations in China. There are obvious seasonal cycles with similar trends among these stations for $CO_2$ fluxes. The fluctuation feature of the $CO_2$ flux at the WLG station in August is probably a result of air mass from the higher

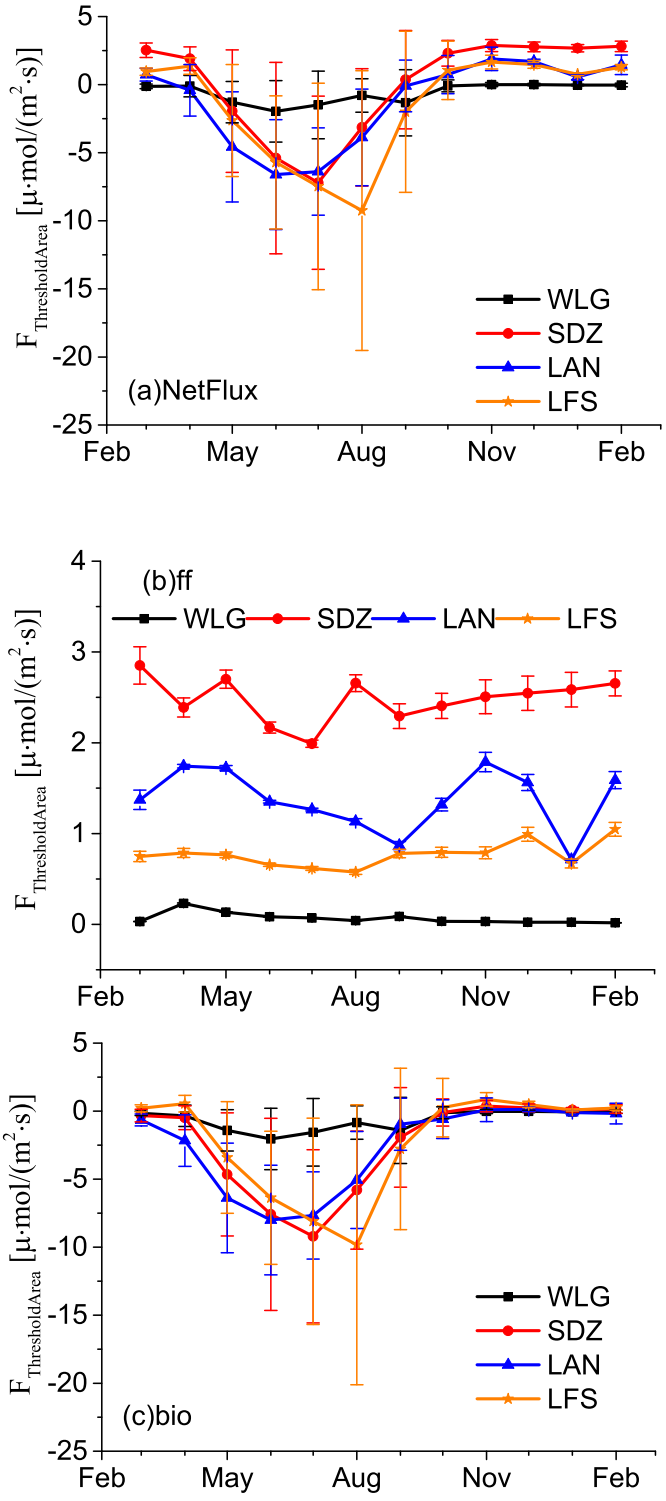


**Fig. 7.** Monthly means and standard deviations of $CO_2$ fluxes from March 2009 to February 2010 in the best threshold area for the four WMO/GAW stations: (a) net fluxes, (b) major source ("ff"), and (c) major sink ("bio"). "ThresholdArea" denotes the best threshold area. "F" denotes fluxes.

emission regions in China. There are greater uncertainties of the $CO_2$ fluxes for these stations between May and September, perhaps partly due to the low-resolution simulation. Overall, WLG is almost a carbon sink in representative area, but the other three regional stations are stronger carbon sources for most of the year from the perspective of fluxes. The uncertainty of the $CO_2$ fluxes is less in representative area of WLG station than that at the other three stations. The strongest and weakest carbon sinks occur at the LFS and WLG stations, respectively. Some differences are found in the time of the strongest carbon sink at the different stations, which is possibly due to the differences of vegetation and growing season.

Additional details can be found by examining the monthly source and sink sectors ("fires," "ff," "bio," and "ocean") in the best threshold area of the four WMO/GAW stations. The contributions of "fires" and "ocean" (not shown in Fig. 7) to the atmospheric $CO_2$ background mole fractions are nearly negligible at each station compared to the influences of fossil fuel burning ("ff", Fig. 7b) and terrestrial biosphere ("bio", Fig. 7c). The seasonal variation of $CO_2$ background mole fraction is controlled mainly by "bio," although there are some seasonal differences in "ff." The "bio" acts mainly as a carbon sink for these stations between May and September. The monthly variations of the "ff" fluxes are larger at SDZ and LAN stations than at the other two stations, which are probably caused by the relatively high regional emissions and sometimes by the air mass from the relatively clean areas, respectively. Compared with the uncertainty of the "ff" flux, the uncertainty of the "bio" flux is larger, playing the dominant role in the uncertainty of the net $CO_2$ flux, especially in the month of the stronger carbon sink. As typical stations, the four stations have very different $CO_2$ source and sink characteristics (Liu et al., 2015). Among the four stations, the bigger uncertainties of the "ff" and "bio" fluxes appear at SDZ and LFS stations, respectively. The intensities of $CO_2$ source and sink are the weakest at WLG as the consequence of less human activity and semi-arid grassland vegetation. The strongest $CO_2$ source of 2.85 μ mol/($m^2$·s) with stronger $CO_2$ sink appear at SDZ, probably because of the Beijing–Tianjin–Hebei economic circle of North China and the shrub vegetation. The $CO_2$ source and sink at LAN are strong, possibly due to the Yangtze River Delta Economic Zone and the hilly lands. The strongest $CO_2$ sink of −9.83 μ mol/($m^2$·s) appears at LFS with weaker source, which might be generated by the forest vegetation and the northeast old industrial base in China. These discrepancies and similarities among the stations indicate that the atmospheric $CO_2$ background mole fractions at the four WMO/GAW stations can play a significant role in understanding regional source–sink characteristics, although it is necessary to reduce the uncertainty of $CO_2$ source and sink in the best threshold region in future's studies.

## 4. Conclusions

This study compared the atmospheric $CO_2$ mole fractions between surface measurement and satellite retrieval at four WMO/GAW stations in China and found the representative areas of the atmospheric $CO_2$ background mole fractions for each station through a statistical method. Additionally, the source and sink in the representative areas were compared. The main findings are summarized below.

The $CO_2$ mole fractions from flask sampling and GOSAT L2 products present similar seasonal patterns at each station from September 2009 to August 2011. For ground-based $CO_2$, the seasonal amplitude (peak-to-peak value) varies in a diminishing sequence from LFS, SDZ, LAN, to WLG. The column-averaged $CO_2$ mole fractions are manifest in the lower amplitude of the seasonal cycle. The extrema of the seasonal $CO_2$ mole fractions from the two datasets are basically synchronous for the specific stations, except a slight phase delay at LAN station. The biggest correlation coefficient ($R' = 0.95$) and the root mean square difference (RMSD = 9.8 ppm) between the two datasets separately appear at SDZ and LFS stations, and the smallest values ($R' = 0.68$, RMSD = 4.4 ppm, and MD = 3.7 ppm) are found at the WLG station.

The distribution of $CO_2$ mole fractions from the GOSAT L3 products over China during September 2009–August 2011 shows significant seasonal difference (low in summer and high in winter) and spatial gradient (low in the western part and high in the eastern part of China). Through the comparison of the two-year averages, column $CO_2$ is found lower than ground-based $CO_2$, but at WLG, both of them have the lowest $CO_2$ mole fraction. The lowest (~4 ppm) and largest (~8 ppm)

differences between the two datasets appear at WLG and LFS stations, respectively. Compared with the winter situation, the $CO_2$ mole fraction and its difference between full column and surface measurement are smaller in summer. The differences of full column $CO_2$ between these stations are also much smaller than their surface observations. In winter, the maximum of ground-based $CO_2$ mole fractions and the greatest difference between the two datasets appear at the LFS station, perhaps due to the winter heating in Northeast China. These varying results are probably induced by uptakes and emissions by vegetation and soils and anthropogenic emissions.

In addition, footprints, which can reflect emission sensitivity, are distributed in different regions for different seasons and sites due to the summer and winter monsoons. The linear regression analysis of flask data and simulated results reveals that the $CO_2$ patterns at these stations can be simulated well by the CT2015 model. The $CO_2$ background mole fractions at the four stations have been extracted from qualified $CO_2$ simulation results by the screening method of Robust Extraction of Background Signal and then smoothed by the curve-fitting method.

While exploring the source–sink regional representativeness of the monthly $CO_2$ fitted background mole fractions at the WMO/GAW stations, representative areas are found using footprints and emissions. Smaller representative areas appear at the SDZ and LFS stations with the larger of the best footprint threshold values, but the opposite case occurs at the WLG and LAN stations. The representative areas are larger in summer than in winter at the WLG and SDZ stations, but the situation is opposite at the LAN and LFS stations. The distributions of best threshold area are significantly different whether in summer or winter or among different stations. The representative areas for $CO_2$ background mole fractions at the WLG, SDZ, LAN, and LFS stations are distributed mainly in the western part of China, the Beijing–Tianjin–Hebei region, the eastern part of China, and northeast China, respectively.

The source and sink in the representative regions were also compared. The flux has obvious seasonal cycles with similar trends but different seasonal variation ranges at the four stations. There are also some differences in the time of strongest carbon sink for the different stations. The intensities of $CO_2$ source and sink are the weakest at WLG; the strongest $CO_2$ source of 2.85 μ mol/($m^2$·s) with stronger $CO_2$ sink occurs at SDZ; the $CO_2$ source and sink at LAN are strong and close to the intensities at SDZ; and the strongest $CO_2$ sink of −9.83 μ mol/($m^2$·s) appears at LFS with weaker source. The uncertainties of the $CO_2$ fluxes are different at different stations in different months and source-sink sectors. Overall, WLG is a carbon sink in the representative area, but the other three stations present stronger carbon sources during the most period of the year. The different atmospheric conditions, vegetation types, and economic zones represented by the four stations contribute to the different sources and sinks in the representative areas. Thus, the atmospheric $CO_2$ background mole fractions at the four WMO/GAW stations in China can play a significant role in understanding regional $CO_2$ source–sink characteristics and patterns over China, although it is necessary to reduce the uncertainty of $CO_2$ source and sink in the best threshold region in future's studies.

## Acknowledgments

This work was supported by the National Natural Science Foundation of China (Grant No. 41505123), the International S&T Cooperation Program of the MOST (Grant No. 2015DFG21960), the National Key Research and Development Program of China (Grant No.2016YFA0601304), and the CAMS Fundamental Research Funds (Grant No. 2015Y002).

We are grateful to all of the staff who work at the WMO/GAW stations in China for collecting the flask air samples, and to the Greenhouse Gases Research Laboratory of the China Meteorological Administration (CMA) for sample analysis. We appreciate Ed Dlugokencky, Andy Crotwell, and Kirk Thoning of NOAA for their support of the research measurements. We also thank the National Oceanic and Atmospheric Administration (NOAA) for providing the CT2015 data, the Norwegian Institute for Air Research for providing the FLEXPART model, and the Japan Aerospace Exploration Agency/National Institute for Environmental Studies/Ministry of the Environment (JAXA/NIES/MOE) for the GOSAT products.

## References

An, X., Yao, B., Li, Y., Li, N., Zhou, L., 2014. Tracking source area of Shangdianzi station using Lagrangian particle dispersion model of FLEXPART. Meteorol. Appl. 21, 466–473.

An, X., Zhou, L., Yao, B., Xu, L., Ma, L., 2012. Analysis on source features of halogenated gases at Shangdianzi regional atmospheric background station. Atmos. Environ. 57, 91–100.

Aumann, H.H., Chahine, M.T., Gautier, C., Goldberg, M., Kalnay, E., McMillin, L., Revercomb, H., Rosenkranz, P.W., Smith, W.L., Staelin, D., Strow, L., Susskind, J., 2003. AIRS/AMSU/HSB on the aqua mission: design, science objectives, data products, and processing systems. IEEE Trans. Geosci. Rem. Sens. 41, 253–264.

Baker, D.F., Bösch, H., Doney, S.C., O'Brien, D., Schimel, D.S., 2010. Carbon source/sink information provided by column $CO_2$ measurements from the Orbiting Carbon Observatory. Atmos. Chem. Phys. 10, 4145–4165.

Ballantyne, A.P., Alden, C.B., Miller, J.B., Tans, P.P., White, J.W., 2012. Increase in observed net carbon dioxide uptake by land and oceans during the past 50 years. Nature 488, 70–72.

Boesch, H., Baker, D., Connor, B., Crisp, D., Miller, C., 2011. Global characterization of $CO_2$ column retrievals from shortwave-infrared satellite observations of the orbiting carbon Observatory-2 mission. Rem. Sens. 3, 270–304.

Bovensmann, H., Burrows, J.P., Buchwitz, M., Frerick, J., Noël, S., Rozanov, V.V., Chance, K.V., Goede, A.P.H., 1999. SCIAMACHY: mission objectives and measurement modes. J. Atmos. Sci. 56, 127–150.

Bréon, F.M., Ciais, P., 2010. Spaceborne remote sensing of greenhouse gas concentrations. Compt. Rendus Geosci. 342, 412–424.

Buchwitz, M., Noël, S., Bramstedt, K., Rozanov, V.V., Eisinger, M., Bovensmann, H., Tsvetkova, S., Burrows, J.P., 2004. Retrieval of trace gas vertical columns from SCIAMACHY/ENVISAT near-infrared nadir spectra: first preliminary results. Adv. Space Res. 34, 809–814.

Chen, X., Wang, J., Liu, Y., Xu, X., Cai, Z., Yang, D., Yan, C.X., Feng, L., 2017. Angular dependence of aerosol information content in CAPI/TanSat observation over land: effect of polarization and synergy with A-train satellites. Rem. Sens. Environ. 196, 163–177.

Cheng, S., An, X., Zhou, L., Tans, P.P., Jacobson, A., 2017a. Atmospheric $CO_2$ at Waliguan station in China: transport climatology, temporal patterns and source-sink region representativeness. Atmos. Environ. 159, 107–116.

Cheng, S., Wang, Y., An, X., 2017b. Temporal variation and source identification of black carbon at Lin'an and Longfengshan regional background stations in China. J. Meteorol. Res. 31, 1070–1084.

Cheng, Y., An, X., Yun, F., Zhou, L., Liu, L., Fang, S., Xu, L., 2013. Simulation of $CO_2$ variations at Chinese background atmospheric monitoring stations between 2000 and 2009: applying a CarbonTracker model. Chin. Sci. Bull. 58, 3986–3993.

Chevallier, F., Deutscher, N.M., Conway, T.J., Ciais, P., Ciattaglia, L., Dohe, S., Fröhlich, M., Gomez-Pelaez, A.J., Griffith, D., Hase, F., Haszpra, L., Krummel, P., Kyrö, E., Labuschagne, C., Langenfelds, R., Machida, T., Maignan, F., Matsueda, H., Morino, I., Notholt, J., Ramonet, M., Sawa, Y., Schmidt, M., Sherlock, V., Steele, P., Strong, K., Sussmann, R., Wennberg, P., Wofsy, S., Worthy, D., Wunch, D., Zimnoch, M., 2011. Global $CO_2$ fluxes inferred from surface air-sample measurements and from TCCON retrievals of the $CO_2$ total column. Geophys. Res. Lett. 38, L24810.

Chevallier, F., Maksyutov, S., Bousquet, P., Bréon, F.M., Saito, R., Yoshida, Y., Yokota, T., 2009. On the accuracy of the $CO_2$ surface fluxes to be estimated from the GOSAT observations. Geophys. Res. Lett. 36, L19807.

Clerbaux, C., Boynard, A., Clarisse, L., George, M., Hadji-Lazaro, J., Herbin, H., Hurtmans, D., Pommier, M., Razavi, A., Turquety, S., Wespes, C., Coheur, P.F., 2009. Monitoring of atmospheric composition using the thermal infrared IASI/MetOp sounder. Atmos. Chem. Phys. 9, 6041–6054.

Cogan, A.J., Boesch, H., Parker, R.J., Feng, L., Palmer, P.I., Blavier, J.F.L., Deutscher, N.M., Macatangay, R., Notholt, J., Roehl, C., Warneke, T., Wunch, D., 2012. Atmospheric carbon dioxide retrieved from the Greenhouse gases Observing SATellite (GOSAT): comparison with ground-based TCCON observations and GEOS-Chem model calculations. J. Geophys. Res. 117, D21301.

Fang, S., Luan, T., Zhang, G., Wu, Y., Yu, D., 2015a. The determination of regional $CO_2$ mole fractions at the Longfengshan WMO/GAW station: a comparison of four data filtering approaches. Atmos. Environ. 116, 36–43.

Fang, S., Tans, P., Steinbacher, M., Zhou, L., Luan, T., 2015b. Comparison of the regional $CO_2$ mole fraction filtering approaches at a WMO/GAW regional station in China. Atmos. Measur. Tech. 8, 5301–5313.

Fang, S., Tans, P.P., Steinbacher, M., Zhou, L., Luan, T., Li, Z., 2016. Observation of atmospheric $CO_2$ and CO at Shangri-La station: results from the only regional station located at southwestern China. Tellus B Chem. Phys. Meteorol. 68, 28506.

Fang, S., Zhou, L., Tans, P., Ciais, P., Steinbacher, M., Xu, L., Luan, T., 2014. In situ measurement of atmospheric $CO_2$ at the four WMO/GAW stations in China. Atmos. Chem. Phys. 14, 2541–2554.

Frankenberg, C., Pollock, R., Lee, R.A.M., Rosenberg, R., Blavier, J.F., Crisp, D., O'Dell, C.W., Osterman, G.B., Roehl, C., Wennberg, P.O., Wunch, D., 2015. The Orbiting Carbon Observatory (OCO-2): spectrometer performance evaluation using pre-launch direct sun measurements. Atmos. Measur. Tech. 8, 301–313.

Houweling, S., Breon, F.M., Aben, I., Rödenbeck, C., Gloor, M., Heimann, M., Ciais, P., 2004. Inverse modeling of $CO_2$ sources and sinks using satellite data: a synthetic

inter-comparison of measurement techniques and their performance as a function of space and time. Atmos. Chem. Phys. 4, 523–538.
IPCC-AR5, 2013. Climate Change 2013: the Physical Science Basis. Working Group I Contribution to the Fifth Assessment Report of the Intergovernmental Panel on Climate Change, Summary for Policymakers.
Jiang, F., Wang, H., Chen, J., Zhou, L., Ju, W., Ding, A., Liu, L., Peters, W., 2013. Nested atmospheric inversion for the terrestrial carbon sources and sinks in China. Biogeosciences 10, 5311–5324.
Jiang, X., Chahine, M.T., Olsen, E.T., Chen, L.L., Yung, Y.L., 2010. Interannual variability of mid-tropospheric $CO_2$ from atmospheric infrared sounder. Geophys. Res. Lett. 37, L13801.
Jiang, X., Crisp, D., Olsen, E., Kulawik, S., Miller, C., Pagano, T., Liang, M., Yung, Y., 2016. $CO_2$ annual and semiannual cycles from multiple satellite retrievals and models. Earth Space Sci. 3, 78–87.
Kulawik, S.S., Jones, D.B.A., Nassar, R., Irion, F.W., Worden, J.R., Bowman, K.W., Machida, T., Matsueda, H., Sawa, Y., Biraud, S.C., Fischer, M.L., Jacobson, A.R., 2010. Characterization of tropospheric emission spectrometer (TES) $CO_2$ for carbon cycle science. Atmos. Chem. Phys. 10, 5601–5623.
Kuze, A., Suto, H., Nakajima, M., Hamazaki, T., 2009. Thermal and near infrared sensor for carbon observation Fourier-transform spectrometer on the Greenhouse Gases Observing Satellite for greenhouse gases monitoring. Appl. Optic. 48, 6716–6733.
Lauvaux, T., Pannekoucke, O., Sarrat, C., Chevallier, F., Ciais, P., Noilhan, J., Rayner, P.J., 2009. Structure of the transport uncertainty in mesoscale inversions of $CO_2$ sources and sinks using ensemble model simulations. Biogeosciences 6, 1089–1102.
Lei, L., Guan, X., Zeng, Z., Zhang, B., Ru, F., Bu, R., 2014. A comparison of atmospheric $CO_2$ concentration GOSAT-based observations and model simulations. Sci. China Earth Sci. 57, 1393–1402.
Li, C., Zhou, L., Qin, D., Liu, L., Qin, X., Wang, Z., Ren, J., 2014. Preliminary study of atmospheric carbon dioxide in a glacial area of the Qilian Mountains, west China. Atmos. Environ. 99, 485–490.
Li, R., Zhang, M., Chen, L., Kou, X., Skorokhod, A., 2017. CMAQ simulation of atmospheric $CO_2$ concentration in East Asia: comparison with GOSAT observations and ground measurements. Atmos. Environ. 160, 176–185.
Liu, D., Lei, L., Guo, L., Zeng, Z., 2015. A cluster of $CO_2$ change characteristics with GOSAT observations for viewing the spatial pattern of $CO_2$ emission and absorption. Atmosphere 6, 1695–1713.
Liu, L., Zhou, L., Vaughn, B., Miller, J., Brand, W., Rothe, M., Xia, L., 2014. Background variations of atmospheric $CO_2$ and carbon-stable isotopes at Waliguan and Shangdianzi stations in China. J. Geophys. Res. Atmos. 119, 5602–5612.
Liu, L., Zhou, L., Zhang, X., Wen, M., Zhang, F., Yao, B., Fang, S., 2009. The characteristics of atmospheric $CO_2$ concentration variation of four national background stations in China. Sci. China Series D Earth Sci. 52, 1857–1863.
Liu, S., Zhou, T., Wei, L., Shu, Y., 2012. The spatial distribution of forest carbon sinks and sources in China. Chin. Sci. Bull. 57, 1699–1707.
Lu, Z., Streets, D., Zhang, Q., Wang, S., 2012. A novel back-trajectory analysis of the origin of black carbon transported to the Himalayas and Tibetan Plateau during 1996-2010. Geophys. Res. Lett. 39, L01809.
Masarie, K., Langenfelds, R., Allison, C., Conway, T., Dlugokencky, E., Francey, R., Novelli, P., Steele, L., Tans, P., Vaughn, B., White, J., 2001. NOAA/CSIRO Flask Air Intercomparison Experiment: a strategy for directly assessing consistency among atmospheric measurements made by independent laboratories. J. Geophys. Res.: Atmos. 106, 20445–20464.
Miao, R., Lu, N., Yao, L., Zhu, Y., Wang, J., Sun, J., 2013. Multi-year comparison of carbon dioxide from satellite data with ground-based FTS measurements (2003–2011). Rem. Sens. 5, 3431–3456.
Miller, C.E., Crisp, D., DeCola, P.L., Olsen, S.C., Randerson, J.T., Michalak, A.M., Alkhaled, A., Rayner, P., Jacob, D.J., Suntharalingam, P., Jones, D.B.A., Denning, A.S., Nicholls, M.E., Doney, S.C., Pawson, S., Boesch, H., Connor, B.J., Fung, I.Y., O'Brien, D., Salawitch, R.J., Sander, S.P., Sen, B., Tans, P., Toon, G.C., Wennberg, P.O., Wofsy, S.C., Yung, Y.L., Law, R.M., 2007. Precision requirements for space-based $X_{CO2}$ data. J. Geophys. Res. 112, D10314.
Nassar, R., Jones, D.B.A., Kulawik, S.S., Worden, J.R., Bowman, K.W., Andres, R.J., Suntharalingam, P., Chen, J.M., Brenninkmeijer, C.A.M., Schuck, T.J., Conway, T.J., Worthy, D.E., 2011. Inverse modeling of $CO_2$ sources and sinks using satellite observations of $CO_2$ from TES and surface flask measurements. Atmos. Chem. Phys. 11, 6029–6047.
O'Dell, C., Connor, B., Bösch, H., O'Brien, D., Frankenberg, C., Castano, R., Christi, M., Eldering, D., Fisher, B., Gunson, M., McDuffie, J., Miller, C., Natraj, V., Oyafuso, F., Polonsky, I., Smyth, M., Taylor, T., Toon, G., Wennberg, P., Wunch, D., 2012. The ACOS $CO_2$ retrieval algorithm – Part 1: description and validation against synthetic observations. Atmos. Measur. Tech. 5, 99–121.
Peters, G., Marland, G., Le Quéré, C., Boden, T., Canadell, J., Raupach, M., 2011. Rapid growth in $CO_2$ emissions after the 2008–2009 global financial crisis. Nat. Clim. Change 2, 2–4.
Peters, W., Jacobson, A., Sweeney, C., Andrews, A., Conway, T., Masarie, K., Miller, J., Bruhwiler, L., Petron, G., Hirsch, A., Worthy, D., van der Werf, G., Randerson, J., Wennberg, P., Krol, M., Tans, P., 2007. An atmospheric perspective on North American carbon dioxide exchange: CarbonTracker. Proc. Natl. Acad. Sci. U. S. A 104, 18925–18930.
Piao, S., Fang, J., Ciais, P., Peylin, P., Huang, Y., Sitch, S., Wang, T., 2009. The carbon balance of terrestrial ecosystems in China. Nature 458, 1009–1013.
Pillai, D., Gerbig, C., Marshall, J., Ahmadov, R., Kretschmer, R., Koch, T., Karstens, U., 2010. High resolution modeling of $CO_2$ over Europe: implications for representation errors of satellite retrievals. Atmos. Chem. Phys. 10, 83–94.
Pu, J., Xu, H., He, J., Fang, S., Zhou, L., 2014. Estimation of regional background concentration of $CO_2$ at Lin'an station in Yangtze River Delta, China. Atmos. Environ. 94, 402–408.
Reuter, M., Bovensmann, H., Buchwitz, M., Burrows, J.P., Connor, B.J., Deutscher, N.M., Griffith, D.W.T., Heymann, J., Keppel-Aleks, G., Messerschmidt, J., Notholt, J., Petri, C., Robinson, J., Schneising, O., Sherlock, V., Velazco, V., Warneke, T., Wennberg, P.O., Wunch, D., 2011. Retrieval of atmospheric $CO_2$ with enhanced accuracy and precision from SCIAMACHY: validation with FTS measurements and comparison with model results. J. Geophys. Res. 116, D04301.
Ruckstuhl, A., Henne, S., Reimann, S., Steinbacher, M., Vollmer, M., O'Doherty, S., Buchmann, B., Hueglin, C., 2012. Robust extraction of baseline signal of atmospheric trace species using local regression. Atmos. Measur. Tech. 5, 2613–2624.
Stohl, A., Forster, C., Frank, A., Seibert, P., Wotawa, G., 2005. Technical note: the Lagrangian particle dispersion model FLEXPART version 6.2. Atmos. Chem. Phys. 5, 2461–2474.
Streets, D., Canty, T., Carmichael, G., de Foy, B., Dickerson, R., Duncan, B., Edwards, D., Haynes, J., Henze, D., Houyoux, M., Jacob, D., Krotkov, N., Lamsal, L., Liu, Y., Lu, Z., Martin, R., Pfister, G., Pinder, R., Salawitch, R., Wecht, K., 2013. Emissions estimation from satellite retrievals: a review of current capability. Atmos. Environ. 77, 1011–1042.
Sun, Z., Wang, X., Yamamoto, H., Tani, H., Zhong, G., Yin, S., 2018. An attempt to introduce atmospheric $CO_2$ concentration data to estimate the gross primary production by the terrestrial biosphere and analyze its effects. Ecol. Indicat. 84, 218–234.
Tangborn, A., Strow, L.L., Imbiriba, B., Ott, L., Pawson, S., 2013. Evaluation of a new middle-lower tropospheric $CO_2$ product using data assimilation. Atmos. Chem. Phys. 13, 4487–4500.
Tans, P., Thoning, K., Elliott, W., Conway, T., 1989. Background Atmospheric $CO_2$ Patterns from Weekly Flask Samples at Barrow, Alaska: Optimal Signal Recovery and Error Estimates, NOAA Technical Memorandum ERL ARL-173. Environmental Research Laboratories, Boulder, pp. 112–131.
Thoning, K., Tans, P., Komhyr, W., 1989. Atmoshperic carbon dioxide at Mauna Loa observatory 2. Analysis of the NOAA GMCC data, 1974-1985. J. Geophys. Res. Atmos. 94, 8549–8565.
Wang, X., Zhang, X., Zhang, L., Gao, L., Tian, L., 2015. Interpreting seasonal changes of low-tropospheric $CO_2$ over China based on SCIAMACHY observations during 2003–2011. Atmos. Environ. 103, 180–187.
Xia, L., Zhou, L., Tans, P., Liu, L., Zhang, G., Wang, H., Luan, T., 2015. Atmospheric $CO_2$ and its $\delta^{13}C$ measurements from flask sampling at Lin'an regional background station in China. Atmos. Environ. 117, 220–226.
Xu, B., Li, J., Liu, Q., Xin, X., Zeng, Y., Yin, G., 2015. Review of methods for evaluating representativeness of ground station observations. J. Rem. Sens. 19, 703–718 (In Chinese with English Abstract).
Xu, J., Wang, Z., Yu, G., Sun, W., Qin, X., Ren, J., Qin, D., 2013. Seasonal and diurnal variations in aerosol concentrations at a high-altitude site on the northern boundary of Qinghai-Xizang Plateau. Atmos. Res. 120–121, 240–248.
Xu, Y., Ke, C., Zhan, W., Li, H., Yao, L., 2017. Variations in satellite-derived carbon dioxide over different regions of China from 2003 to 2011. Atmos. Environ. 150, 379–388.
Yokota, T., Yoshida, Y., Eguchi, N., Ota, Y., Tanaka, T., Watanabe, H., Maksyutov, S., 2009. Global concentrations of $CO_2$ and $CH_4$ retrieved from GOSAT: first preliminary results. Sola 5, 160–163.
Yoshida, Y., Ota, Y., Eguchi, N., Kikuchi, N., Nobuta, K., Tran, H., Morino, I., Yokota, T., 2011. Retrieval algorithm for $CO_2$ and $CH_4$ column abundances from short-wavelength infrared spectral observations by the Greenhouse gases observing satellite. Atmos. Measur. Tech. 4, 717–734.
Zhang, F., Zhou, L., Conway, T., Tans, P., Wang, Y., 2013a. Short-term variations of atmospheric $CO_2$ and dominant causes in summer and winter: analysis of 14-year continuous observational data at Waliguan, China. Atmos. Environ. 77, 140–148.
Zhang, F., Zhou, L., 2013. Implications for $CO_2$ emissions and sinks changes in western China during 1995–2008 from atmospheric $CO_2$ at Waliguan. Tellus B 65, 19576.
Zhang, H., Chen, B., Machida, T., Matsueda, H., Sawa, Y., Fukuyama, Y., Langenfelds, R., van der Schoot, M., Xu, G., Yan, J., Cheng, M., Zhou, L., Tans, P., Peters, W., 2014a. Estimating Asian terrestrial carbon fluxes from CONTRAIL aircraft and surface $CO_2$ observations for the period 2006-2010. Atmos. Chem. Phys. 14, 5807–5824.
Zhang, H., Chen, B., van der Laan-Luijkx, I., Chen, J., Xu, G., Yan, J., Zhou, L., Fukuyama, Y., Tans, P., Peters, W., 2014b. Net terrestrial $CO_2$ exchange over China during 2001-2010 estimated with an ensemble data assimilation system for atmospheric $CO_2$. J. Geophys. Res.: Atmos. 119, 3500–3515.
Zhang, J., Wang, C., Liu, L., Guo, H., Liu, G., Li, Y., Deng, S., 2014c. Investigation of carbon dioxide emission in China by primary component analysis. Sci. Total Environ. 472, 239–247.
Zhang, L., Jiang, H., Zhang, X., 2015. Comparison analysis of the global carbon dioxide concentration column derived from SCIAMACHY, AIRS, and GOSAT with surface station measurements. Int. J. Rem. Sens. 36, 1406–1423.
Zhang, Z., Jiang, H., Liu, J., Ju, W., Zhang, X., 2013b. Effect of heterogeneous atmospheric $CO_2$ on simulated global carbon budget. Global Planet. Change 101, 33–51.
Zhou, C., Shi, R., Liu, C., Gao, W., 2013. A correlation analysis of monthly mean $CO_2$ retrieved from the Atmospheric Infrared Sounder with surface station measurements. Int. J. Rem. Sens. 34, 8710–8723.
Zhou, L., Conway, T., White, J., Mukai, H., Zhang, X., Wen, Y., Li, J., MacClune, K., 2005. Long-term record of atmospheric $CO_2$ and stable isotopic ratios at Waliguan Observatory: background features and possible drivers, 1991-2002. Global Biogeochem. Cycles 19, GB3021.
Zhou, L., Tang, J., Wen, Y., Yan, P., Li, J., Zhang, X., 2003. The impact of local winds and long-range transport on the continuous carbon dioxide record at Mount Waliguan, China. Tellus B 55, 145–158.
Zhou, L., White, J., Conway, T., Mukai, H., MacClune, K., Zhang, X., Wen, Y., Li, J., 2006. Long-term record of atmospheric $CO_2$ and stable isotopic ratios at Waliguan Observatory: seasonally averaged 1991-2002 source/sink signals, and a comparison of 1998-2002 record to the 11 selected sites in the Northern Hemisphere. Global Biogeochem. Cycles 20, GB2001.